Impact of Different AC Voltage Control Modes of Wind-farm-side MMC on Stability of MMC-HVDC with Offshore Wind Farms

Hongfei Lin, Tao Xue, Jing Lyu, and Xu Cai

***Abstract*—Wind-farm-side modular multilevel converters (WFMMCs) used in modular multilevel converter based high-voltage direct current (MMC-HVDC) transmission systems must be able to control the AC grid voltage in offshore wind farms. Different AC voltage control strategies can significantly affect the dynamic characteristics of WFMMCs. However, existing studies have not provided a general methodology of controller parameter design, and few comparative studies have been conducted on control performance under varying operating conditions as well as the effects of different AC voltage control modes (AVCMs) on the stability of MMC-HVDCs with offshore wind farms. This paper provides a controller parameter design method for AVCMs, which is tested in various operating scenarios. Sequence impedance models of offshore wind farms and WFMMCs under different AVCMs are then developed. The effects of AVCMs on the small-signal stability of the interconnected system are then analyzed and compared using the impedance-based method. Finally, case studies are conducted on a practical MMC-HVDC system with offshore wind farms to verify the theoretical analysis.**

***Index Terms*—Offshore wind farm, modular multilevel converter based high-voltage direct current (MMC-HVDC), AC voltage control, stability, dynamic response characteristics.**

I. Introduction

WIND power, as a major type of renewable energy, has been exploited worldwide in both onshore and offshore wind farms [1], [2]. In recent years, offshore wind power has become a critical component of wind-energy development. Increasingly, offshore wind farms are being built on a large scale and remote from the shore, where wind power must then be collected by cables and transported to onshore grids across great distances [3]. Modular multilevel converter based high-voltage direct current (MMC-HVDC) has become the prevailed scheme for remote offshore wind farms [4], [5].

The wind-farm-side MMC (WFMMC) station of an MMC-HVDC transmission system is the terminal to which offshore wind farms are connected. Based on [6], a primary responsibility of the WFMMC is to provide an offshore grid voltage to serve as a reference voltage for the wind turbine. AC voltage control modes (AVCMs) significantly affect the dynamic characteristics of the WFMMC, and the stability risks of wideband oscillations in the offshore WFMMC interconnected system are exacerbated when using improper control techniques and parameters [7]. The AVCMs of WFMMCs can generally be classified into three types: open-loop [8], single-loop with AC voltage control [9], and double-loop with an outer AC voltage loop and a current inner loop [10]. Most studies have investigated the small-signal stability of grid integration of offshore wind farms with MMC-HVDCs based on specific types of WFMMC control. Eigenvalue- and impedance-based methods are effective tools for studying these small-signal stability issues. The eigenvalue-based method requires building the state-space model of the entire system, including all components, and obtaining the state matrix, where the order of the state-space model and computation burden can be considerably high. In addition, the state-space model must be updated with system structural modifications, making it unsuitable for practical analysis. Due to its simplicity and extensibility, the impedance stability analytical method is widely applicable to address oscillation problems derived from interactions between power converters.

For open-loop-controlled WFMMCs, sequence impedance models have been developed using both the harmonic state-space method [8] and multi-harmonic linearization method [11]. Internal dynamics in the MMC have been shown to be the dominant factors of sub-/super-synchronous oscillations in MMC-HVDC-connected wind farms [2], [12]. The open-loop-controlled MMC is easy to implement but does not have auxiliary functions (e. g., grid support and fault ride-through). Therefore, closed-loop control of the WFMMC is preferred in practical systems. A proportional-resonant (PR) controller has been utilized in previous studies [8], [9],

Manuscript received: June 22, 2022; revised: September 14, 2022; accepted: December 8, 2022. Date of CrossCheck: December 8, 2022. Date of online publication: January 25, 2023.

This work was supported by the National Natural Science Foundation of China (No. 51907125).

H. Lin, J. Lyu (corresponding author), and X. Cai are with the Key Laboratory of Control of Power Transmission and Conversion, Ministry of Education, Department of Electrical Engineering, Shanghai Jiao Tong University, Shanghai 200240, China (e-mail: lhfnbo@sjtu.edu.cn; lvjing@sjtu.edu.cn; xucai@sjtu.edu.cn).

T. Xue was with the Department of Electrical Engineering, Shanghai Jiao Tong University, Shanghai, China, and he is also with the Department of Electrical Engineering, The Hong Kong Polytechnic University, Hong Kong, China (e-mail: xt-tao.xue@connect.polyu.hk).

DOI: 10.35833/MPCE.2022.000363

where the parameters can be adjusted to stabilize the MMC system. However, the PR controller generates a higher computational burden, and therefore the proportional-integral (PI) controller has remained the main controller type used in WFMMC control. Reference [13] compares the effects of single- and open-loop-controlled WFMMCs on the stability of interconnected systems. A multi-input multi-output (MIMO) impedance model of a double-loop-controlled WFMMC is built, and the stability of an MMC-HVDC-connected doubly-fed induction generator (DFIG) wind farm is analyzed in [14]. DC-side stability of double-loop-controlled WFMMCs for wind farm integration is analyzed in [15] and [16].

The aforementioned studies did not provide a general parameter design methodology and did not conduct performance comparisons of different AVCMs under varying operating conditions. In addition, comprehensive comparative studies on the effects of different AVCMs on the stability of offshore WFMMC systems have not been conducted. The following four contributions of this study are noteworthy. ① A general control system design methodology based on the bandwidth and turning frequency of the PI controller for a WFMMC control system is illustrated. ② Dynamic performances of different AVCMs under varying operating conditions are compared. ③ The effects of different AVCMs on the wideband oscillations of an interconnected system are analyzed and compared. ④ The advantages of WFMMC control are shown as a reference for industrial practice.

The remainder of this paper is organized as follows. Section II presents the system configuration and control. Section III describes the controller parameter design of different AVCMs. Section IV presents the impedance modeling of wind farm and WFMMC. Section V describes the impacts of different AVCMs on the stability of the interconnected system. Section VI concludes this paper.

II. System Configuration and Control

A. System Configuration

Figure 1 shows the structure of an offshore wind farm with an MMC-HVDC system. Three offshore wind farms are connected to the onshore AC grid via an MMC-HVDC transmission system. The WFMMC and grid-side MMC (GSMMC) comprise the MMC-HVDC system. During normal operation, the WFMMC uses AC voltage control to maintain a steady AC voltage reference for the wind farm at the point of common coupling (PCC). The GSMMC is responsible for maintaining a constant DC voltage and for supporting the AC grid.

This paper primarily focuses on the interactive stability of the shaded region shown in Fig. 1. Based on the assumption that the onshore AC grid is sufficiently strong, the GSMMC can maintain a constant DC voltage. In this case, the effect of the GSMMC on the dynamic stability of the offshore AC grid can be ignored [4]. Alternatively, a constant-voltage DC source can be used to replace the GSMMC. Finally, each wind farm is aggregated into an equivalent wind-turbine generator.

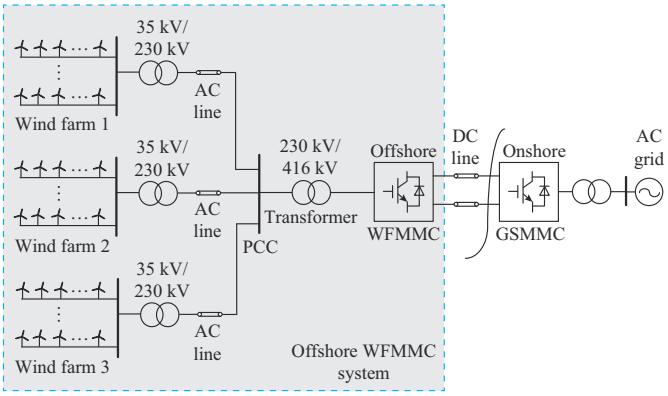

Fig. 1. Structure of an offshore wind farm with an MMC-HVDC system.

The typical configuration of a WFMMC is illustrated in Fig. 2, where the subscripts a, b, c represent three phases; the subscripts u and l represent the upper and lower bridge arms, respectively; m_u and m_l are the modulation functions; $u_{cu\Sigma}$ and $u_{cl\Sigma}$ are the sum voltages of the upper and lower bridge arm sub-module (SM) capacitors, respectively; i_{com} is the circulating current; i_u and i_l are the corresponding arm currents; U_{dc} and i_{dc} are the DC-side voltage and current, respectively; C_{arm} is the capacitance; and u_g and i_g are the AC-side voltage and current, respectively. Each phase of the MMC is divided into upper and lower bridge arms, where each arm contains N SMs, an inductance L_{arm}, and a resistance R_{arm}.

B. System Control

The control diagrams for different AVCMs of WFMMC are shown in Fig. 3. Three AVCMs can be used to provide steady offshore AC voltage: open-loop AVCM (AVCM1), single-loop AVCM (AVCM2), and double-loop AVCM (AVCM3). Note that any variable denoted with a superscript * refers to the reference value. $H_{vac}(s)$, $H_c(s)$, and $H_{cc}(s)$ are the PI controllers in the voltage outer loop, current inner loop, and circulating current suppression control (CCSC), respectively; u^*_{diff} and u^*_{com} are the differential-mode and common-mode voltage reference values, respectively; ω is the fundamental angular frequency, which is $2\pi \times 50$ Hz in this paper; and $L = L_{arm}/2$ represents the inductance of the bridge arm equivalent to the AC side. Other variables are defined in Supplementary Material. VCM1 operates by directly setting a voltage reference wave to control the WFMMC. The main difference between the AVCM2 and AVCM3 is that AVCM3 contains a current inner loop (as compared with an outer AC voltage loop) and has a better current response. In addition, the CCSC is considered to suppress the second-harmonic circulating current within the MMC.

III. Controller Parameter Design of Different AVCMs

Figure 4 shows the structure diagram of the closed-loop control system of the WFMMC with AVCM2 and AVCM3, respectively, where G_{PWM} is the pulse-width modulation gain; U^*_{gdq} is dq-axis grid voltage; and Z_L is the AC-side equivalent load. Note that the common variables are provided in the Supplementary Material.

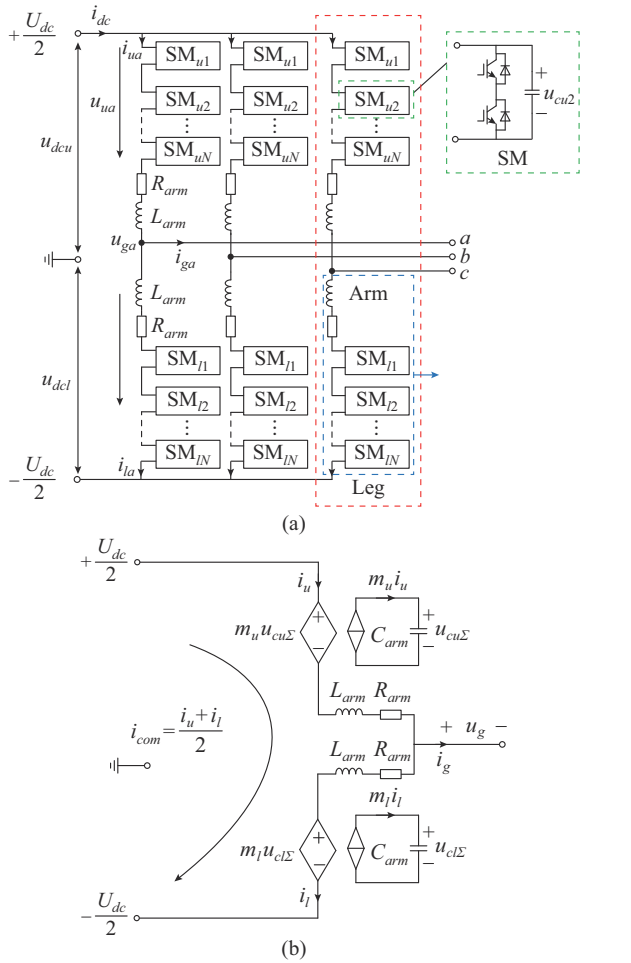

Fig. 2. Typical configuration of a WFMMC. (a) Topology of an MMC. (b) Equivalent circuit of a single-phase MMC leg.

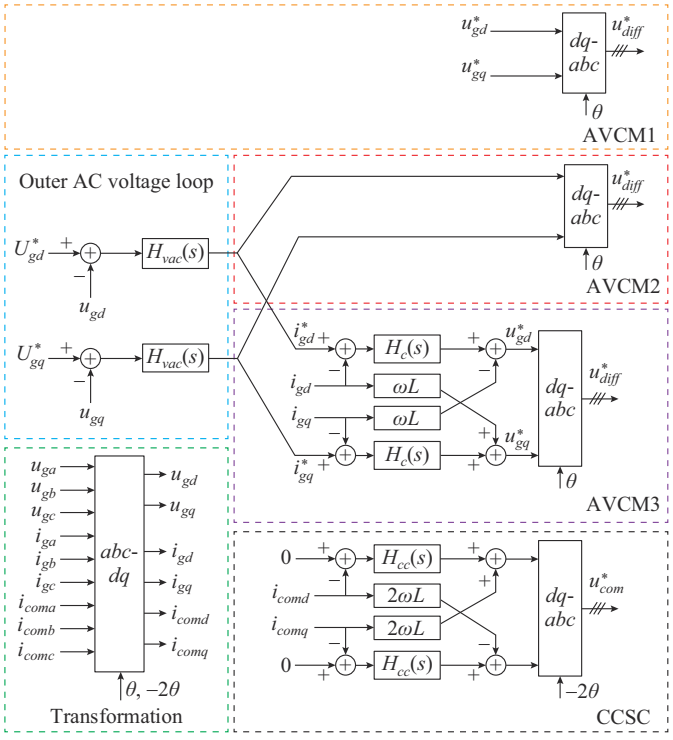

Fig. 3. Control diagrams for different AVCMs of WFMMC.

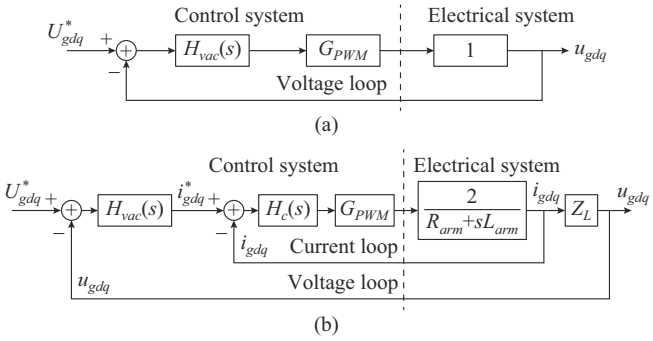

Fig. 4. Structure diagram of closed-loop control system of WFMMC. (a) AVCM2. (b) AVCM3.

The controlled object of AVCM3 is correlated with the impedance characteristics of the load (i. e., the wind farm in this paper), whereas the plant of AVCM2 is irrelevant to the load. This is the main difference in the controller parameter design of the two AVCMs.

A. Parameter Design of AVCM2

For AVCM2, the closed-loop transfer function of the control system is expressed as:

$$H_{cl,single}(s)=\frac{K_{pvs}+\dfrac{K_{ivs}}{s}}{1+\underbrace{K_{pvs}+\dfrac{K_{ivs}}{s}}_{H_{vac}}}=\frac{T_{vs}s+1}{(a_{vs}+T_{vs})s+1} \tag{1}$$

where K_{pvs} and K_{ivs} are the proportional and integral coefficients of the AC voltage PI controller, respectively. The variables are defined by:

$$\begin{cases} a_{vs}=\dfrac{1}{K_{ivs}} \\ T_{vs}=\dfrac{K_{pvs}}{K_{ivs}} \end{cases} \tag{2}$$

where T_{vs} is the turning time of the PI controller. A reciprocal of 10-20 times the cutoff angular frequency is usually required.

The closed-loop bandwidth in the control system is defined as the corresponding bandwidth when the amplitude-frequency characteristic of the closed-loop transfer function is reduced to −3 dB, when its gain is $1/\sqrt{2}$. Therefore, when AVCM2 is adopted, the formula for the AC voltage control-loop transfer function at closed-loop bandwidth ω_b can be derived as:

$$\begin{cases} H_{cl,single}(s)=\dfrac{T_{vs}s+1}{(a_{vs}+T_{vs})s+1}\overset{s=j\omega_b}{=}\dfrac{1+jT_{vs}\omega_b}{1+j\omega_b(a_{vs}+T_{vs})} \\ \left|H_{cl,single}(s)\right|=\dfrac{\sqrt{1+(T_{vs}\omega_b)^2}}{\sqrt{1+\omega_b^2(a_{vs}+T_{vs})^2}}=\dfrac{1}{\sqrt{2}} \end{cases} \tag{3}$$

When (3) is solved, the relationship between a_{vs} and the closed-loop bandwidth ω_b can be obtained as:

$$a_{vs}=-T_{vs}+\sqrt{2T_{vs}^2+\frac{1}{\omega_b^2}} \tag{4}$$

Therefore, the parameters of the outer-loop voltage con-

troller can be calculated by:

$$\begin{cases} K_{ivs} = \dfrac{1}{-T_{vs} + \sqrt{2T_{vs}^2 + \dfrac{1}{\omega_b^2}}} \\ K_{pvs} = K_{ivs} T_{vs} \end{cases} \tag{5}$$

B. Parameter Design of AVCM3

1) Inner-loop Current Controller

For AVCM3, the control parameters of the inner-loop current controller are first designed. When we ignore the decoupling term, the closed-loop transfer function of the inner-loop current controller can be derived as:

$$H_{cl,double}(s) = \frac{\left(K_{pil} + \dfrac{K_{iil}}{s}\right)\dfrac{2}{R_{arm} + sL_{arm}}}{1 + \underbrace{\left(K_{pil} + \dfrac{K_{iil}}{s}\right)}_{H_c}\dfrac{2}{R_{arm} + sL_{arm}}} \approx \frac{\dfrac{2K_{pil}}{L_{arm}}s + \dfrac{2K_{iil}}{L_{arm}}}{s^2 + \dfrac{2K_{pil}}{L_{arm}}s + \dfrac{2K_{iil}}{L_{arm}}} \tag{6}$$

where K_{pil} and K_{iil} are the proportional and integral coefficients of the current PI controller, respectively. Equation (6) can be regarded as a second-order damped system as:

$$G(s) = \frac{2\zeta\omega_n s + \omega_n^2}{s^2 + 2\zeta\omega_n s + \omega_n^2} \tag{7}$$

where ζ and ω_n are the damping ratio and natural frequency, respectively.

Similar to (3), the current control-loop transfer function at the closed-loop bandwidth ω_{bi} in AVCM3 can be derived as:

$$\begin{cases} G(s) = \dfrac{2\zeta\omega_n s + \omega_n^2}{s^2 + 2\zeta\omega_n s + \omega_n^2} \overset{s=\mathrm{j}\omega_{bi}}{=} \dfrac{\omega_n^2 + \mathrm{j}2\zeta\omega_n\omega_{bi}}{\omega_n^2 - \omega_{bi}^2 + \mathrm{j}2\zeta\omega_n\omega_{bi}} \\ \omega_n = \omega_{bi}\sqrt{\sqrt{(2\zeta^2+1)^2+1} - (2\zeta^2+1)} \end{cases} \tag{8}$$

When (6)-(8) are combined, the parameters of the inner-loop current controller can be calculated by:

$$\begin{cases} K_{pil} = \zeta L_{arm}\omega_{bi}\sqrt{\sqrt{(2\zeta^2+1)^2+1} - (2\zeta^2+1)} \\ K_{iil} = \dfrac{L_{arm}}{2}\omega_{bi}^2\sqrt{\sqrt{(2\zeta^2+1)^2+1} - (2\zeta^2+1)} \end{cases} \tag{9}$$

2) Outer-loop Voltage Controller

Because the closed-loop bandwidth of the inner-loop current controller is usually 10-20 times the outer-loop voltage controller, it can be ignored when designing the parameters of the outer-loop voltage controller. The closed-loop transfer function of the outer-loop voltage controller is:

$$H_{clo,double}(s) = \frac{\left(K_{pvl} + \dfrac{K_{ivl}}{s}\right)Z_L}{1 + \underbrace{\left(K_{pvl} + \dfrac{K_{ivl}}{s}\right)}_{H_{vac}}Z_L} \tag{10}$$

Unlike AVCM2, the closed-loop transfer function of AVCM3 contains Z_L. Therefore, the outer-loop control parameters are designed using (11).

$$\begin{cases} K_{ivl} = \dfrac{1}{Z_L\left(-T_{vs} + \sqrt{2T_{vs}^2 + \dfrac{1}{\omega_b^2}}\right)} \\ K_{pvl} = K_{ivl} T_{vs} \end{cases} \tag{11}$$

C. Dynamic Performance Verification of Control System

A time-domain simulation model of WFMMC has been constructed in this paper to assess the dynamic performance of the control system. The main electrical parameters of the WFMMC are listed in Table I. The outer- and inner-loop voltage control bandwidths are set to be 15 Hz and 200 Hz, respectively, and the controller parameters can be calculated using (5), (9), and (11).

TABLE I
MAIN ELECTRICAL PARAMETERS OF WFMMC

Type	Parameter	Value
Electrical system	Rated power	1100 MW
	Rated AC voltage	416 kV
	Rated DC voltage	±400 kV
	SM number in one leg	50
	SM capacitor	11 mF
	Arm inductance	133 mH
MMC transformer (2 in parallel parameters of one device)	Rated power S_{tmmc}	850 MVA
	Connection type	D/Yg
	Ratio	416 kV/230 kV
	Iron loss	0.017 p.u.
	Copper loss	0.0056 p.u.

The reference value of the *d*-axis voltage of the control system is reduced from 1 p.u. to 0.8 p.u. at 1 s, and the dynamic responses of the control system are shown in Fig. 5, where U_{sdq} and I_{sdq} represent *dq*-axis voltages and currents, respectively. The voltages and currents under both AVCMs with the designed parameters exhibit good dynamic performance. In addition, compared with AVCM2, AVCM3 has a better dynamic response speed when the load active power is 100% of the rated power.

According to (5) and (11), the bandwidth of the voltage outer loop under AVCM3 is affected by Z_L, whereas it has little influence under AVCM2. However, the controller parameters in an actual system generally cannot be easily changed. Therefore, studying the dynamic responses of the control system when the load changes is essential. Figure 6 illustrates the impacts of different AVCMs on the dynamic responses under 20%, 60%, and 100% of the rated power.

Note that the change in U_{sd} reference is the same as previously. The responses of the *q*-axis voltage and current per unit value are similar to those of the *d*-axis, which are not shown due to space restrictions. As the load power decreases, the control effects under AVCM3 worsen, whereas they are less affected under AVCM2.

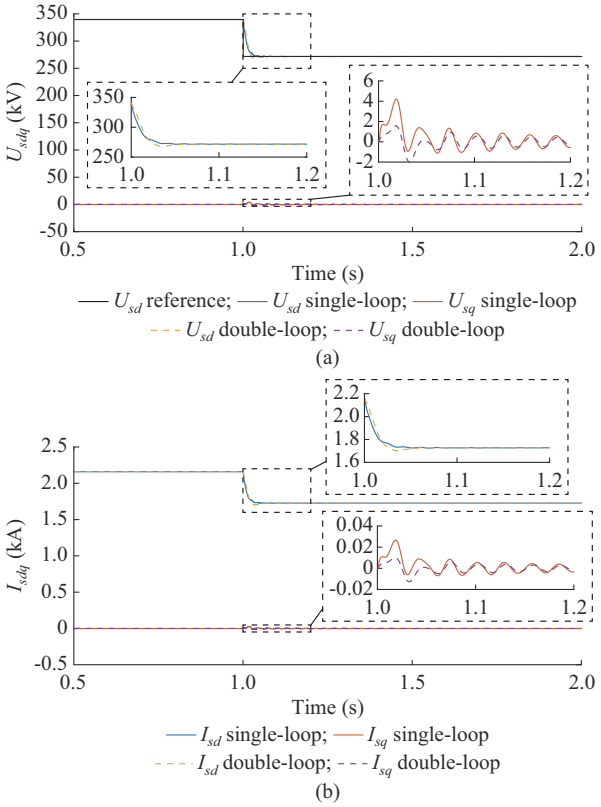

Fig. 5. Dynamic responses of control system. (a) *dq*-axis voltages. (b) *dq*-axis currents.

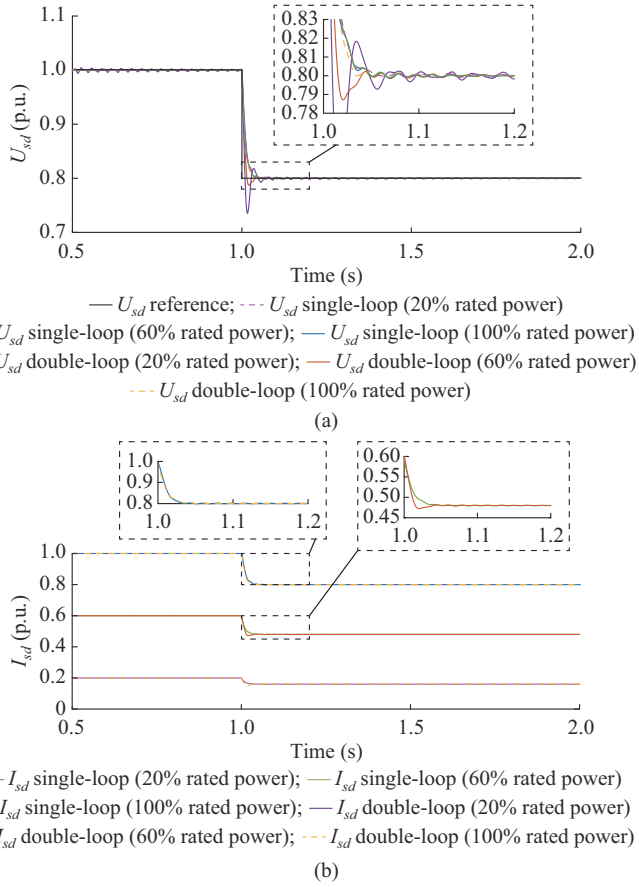

Fig. 6. Impacts of different AVCMs on dynamic responses under 20%, 60%, and 100% of rated power. (a) *d*-axis voltages. (b) *d*-axis currents.

IV. Impedance Modeling of Wind Farm and WFMMC

A. Impedance Modeling of a Wind Farm

An offshore wind farm consists of permanent magnet synchronous generator-based full-power wind turbine systems (PMSG-based FPWTSs). We use a PMSG-based FPWTS as an example, where the system structure is consistent with that in [17], and the main parameters in Fig. 7 are listed in the Supplementary Material. The key modeling processes are as follows.

As Fig. 7 shows, the PMSG-based FPWTS is divided into four SMs (SM1-SM4) with multi-port characteristics for modeling, and the SMs are then connected according to the electrical connection between the ports to obtain the wind farm AC-side load Z_{acW}.

First, SM1 includes a wind turbine and generator. Based on the electromagnetic transient time scale considered in this paper, the aerodynamic and mechanical characteristics of wind turbines can be ignored. Under the assumption that the wind speed is constant, SM1 needs to consider only generator dynamics. The small-signal linearization equation of synchronous generator can be given as:

$$\begin{bmatrix} \tilde{V}_{1d} \\ \tilde{V}_{1q} \end{bmatrix} = \boldsymbol{Z}_{1dq} \begin{bmatrix} \tilde{I}_{1d} \\ \tilde{I}_{1q} \end{bmatrix} \tag{12}$$

where V_{1d}, V_{1q} and I_{1d}, I_{1q} are the generator output voltages and currents in the *dq* axes, respectively; and $\boldsymbol{Z}_{1dq}$ is the *dq*-axis impedance of the generator, where the details related to its form are provided in the Supplementary Material. Note that the variables indicated by tildes represent small-signal forms.

SM2 represents the machine-side converter (MSC), which is connected to the generator and DC bus, and its voltage-current relationship can be described by a two-port model as:

$$\begin{bmatrix} -\tilde{I}_{2d} \\ -\tilde{I}_{2q} \\ \tilde{I}_{2dc} \end{bmatrix} = \underbrace{\begin{bmatrix} \boldsymbol{Y}_{2dq} & \boldsymbol{Y}_{a} \\ \boldsymbol{Y}_{b} & Y_{2dc} \end{bmatrix}}_{\boldsymbol{Y}_{2m\times 2m}} \begin{bmatrix} -\tilde{V}_{2d} \\ -\tilde{V}_{2q} \\ \tilde{V}_{2dc} \end{bmatrix} \tag{13}$$

where V_{2d}, V_{2q} and I_{2d}, I_{2q} are the MSC AC-side voltages and currents in the *dq* axes, respectively; and V_{2dc} and I_{2dc} are the MSC DC-side voltage and current, respectively. The details of $\boldsymbol{Y}_{2m\times 2m}$ are provided in the Supplementary Material.

SM3 is the DC-bus capacitor of the full-power wind turbine, which is connected to the MSC and grid-side converter (GSC). The relationship between the small-signal voltage and current can be described by the KCL equation:

$$\tilde{I}_{2dc} + \tilde{I}_{4dc} + sC_{dc}\tilde{V}_{3dc} = 0 \tag{14}$$

where C_{dc} is the DC-side capacitance; I_{4dc} is the GSC DC-side current; and V_{3dc} is the DC-bus voltage.

Similarly, SM4 represents the GSC and its filter, which is connected to the AC grid and DC bus, and its voltage-current relationship can be described by a two-port model as:

$$\begin{bmatrix} -\tilde{I}^{s}_{4d} \\ -\tilde{I}^{s}_{4q} \\ \tilde{I}_{4dc} \end{bmatrix} = \underbrace{\begin{bmatrix} \boldsymbol{Y}_{4dq} & \boldsymbol{Y}_{c} \\ \boldsymbol{Y}_{d} & Y_{4dc} \end{bmatrix}}_{\boldsymbol{Y}_{2g\times 2g}} \begin{bmatrix} -\tilde{V}^{s}_{4id} \\ -\tilde{V}^{s}_{4iq} \\ \tilde{V}_{4dc} \end{bmatrix} \tag{15}$$

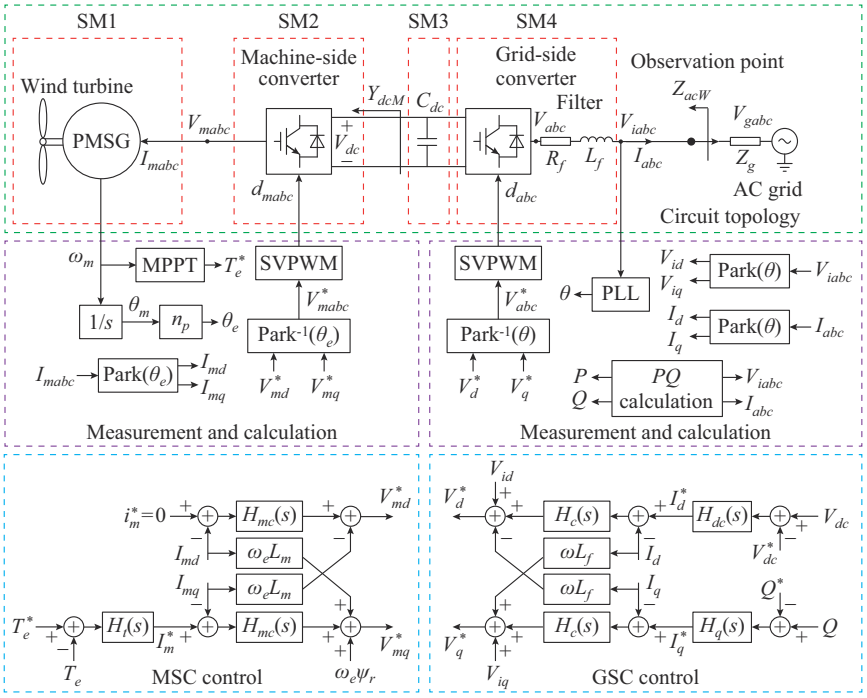

Fig. 7. Topology and control of a PMSG-based FPWTS.

where V_{4id}, V_{4iq} and I_{4d}, I_{4q} are the AC-side voltages and currents of the GSC in the *dq* domain, respectively; and V_{4dc} is the GSC DC-side voltage. Note that the variables denoted with a superscript *s* represent their forms in the electrical coordinate system, and the details of $\boldsymbol{Y}_{2g\times 2g}$ are provided in the Supplementary Material.

1) DC-side Admittance Modeling

After the multiport model of each SM is established, the second step is to connect SM1 and SM2 and convert them into a DC-side admittance. Because the AC ports of SM1 and SM2 are common points, the voltage and current satisfy:

$$\begin{cases}\begin{bmatrix}\tilde{V}_{1d}\\ \tilde{V}_{1q}\end{bmatrix}=\begin{bmatrix}\tilde{V}_{2d}\\ \tilde{V}_{2q}\end{bmatrix}\\ \begin{bmatrix}\tilde{I}_{1d}\\ \tilde{I}_{1q}\end{bmatrix}=\begin{bmatrix}\tilde{I}_{2d}\\ \tilde{I}_{2q}\end{bmatrix}\end{cases} \tag{16}$$

When (16) is substituted into (13), the coupling relationship between the MSC AC and DC voltages can be obtained as:

$$-(\boldsymbol{Z}_{1dq}+\boldsymbol{Y}_{2dq}^{-1})\begin{bmatrix}\tilde{V}_{2d}\\ \tilde{V}_{2q}\end{bmatrix}=\boldsymbol{Y}_a\tilde{\boldsymbol{V}}_{2dc} \tag{17}$$

The DC-side admittance $\boldsymbol{Y}_{dcM}$ can then be calculated by substituting (17) into (13).

$$\begin{cases}-(\boldsymbol{Z}_{1dq}+\boldsymbol{Y}_{2dq}^{-1})\begin{bmatrix}\tilde{V}_{2d}\\ \tilde{V}_{2q}\end{bmatrix}=\boldsymbol{Y}_a\tilde{V}_{2dc}\\ \tilde{I}_{2dc}=\underbrace{\left[\boldsymbol{Y}_{2dc}-\boldsymbol{Y}_b(\boldsymbol{Z}_{1dq}+\boldsymbol{Y}_{2dq}^{-1})^{-1}\boldsymbol{Y}_a\right]}_{\boldsymbol{Y}_{dcM}}\tilde{V}_{2dc}\end{cases} \tag{18}$$

2) AC-side Impedance Modeling

After the equivalent DC-side admittance of the machine-side system is established, the next step is to connect SM3 and SM4 equivalently to the AC-side observation point. Because the DC-bus capacitance is the common point of SM2-SM4, the following voltage equation is established:

$$\tilde{V}_{2dc}=\tilde{V}_{3dc}=\tilde{V}_{4dc} \tag{19}$$

When (18) and (19) are substituted into (14), the updated formula is:

$$\tilde{I}_{4dc}+(Y_{dcM}+sC_{dc})\tilde{V}_{4dc}=0 \tag{20}$$

Then, when (20) is substituted into (15), the coupling relationship between the GSC AC and DC voltages can be obtained as:

$$-(Y_{4dc}+Y_{dcM}+sC_{dc})\tilde{V}_{4dc}=\boldsymbol{Y}_d\begin{bmatrix}\tilde{V}_{4id}^{s}\\ \tilde{V}_{4iq}^{s}\end{bmatrix} \tag{21}$$

Finally, the AC-side impedance $\boldsymbol{Z}_{acW}$ can be calculated by substituting (21) into (15):

$$\begin{bmatrix}\tilde{V}_{4id}^{s}\\ \tilde{V}_{4iq}^{s}\end{bmatrix}=-\underbrace{\left[Y_{4dq}-Y_c(sC_{dc}+Y_{dcM}+Y_{4dc})^{-1}Y_d\right]}_{\boldsymbol{Z}_{acW}}\begin{bmatrix}\tilde{I}_{4d}^{s}\\ \tilde{I}_{4q}^{s}\end{bmatrix} \tag{22}$$

This AC-side impedance is *dq* impedance, which is an MIMO impedance. It can be transformed into a single-input single-output sequence impedance, which is consistent with the literature and is thus not repeated here.

The three wind farms considered in the actual project have 100, 67, and 100 PMSG-based wind turbine generators, respectively, and each wind farm is then aggregated using one equivalent wind turbine generator.

B. Impedance Modeling of WFMMC

1) Impedance Modeling of WFMMC Under AVCM1

The harmonic state space based (HHS-based) impedance modeling of WFMMC is previously elaborated in [8], and therefore the derivation is omitted here. Based on the average value model, with i_{com}, $u_{cu\Sigma}$, $u_{cl\Sigma}$, and i_g used as state variables, the state-space equation of the WFMMC is derived as:

$$\dot{\boldsymbol{x}}^{ss}(t)=\boldsymbol{A}^{ss}(t)\boldsymbol{x}^{ss}(t)+\boldsymbol{B}^{ss}(t)\boldsymbol{u}^{ss}(t) \tag{23}$$

where $\dot{\boldsymbol{x}}^{ss}(t)$ is the derivative of $\boldsymbol{x}^{ss}(t)$. The details of the matrices $\boldsymbol{x}^{ss}(t)$, $\boldsymbol{A}^{ss}(t)$, $\boldsymbol{B}^{ss}(t)$, and $\boldsymbol{u}^{ss}(t)$ are provided in the Supplementary Material.

The form of modulation ratios $\boldsymbol{m}_u$ and $\boldsymbol{m}_l$ can be expressed as:

$$\begin{cases}\boldsymbol{m}_u=\dfrac{\boldsymbol{u}^*_{com}-\boldsymbol{u}^*_{diff}}{V_{dc}}\\ \boldsymbol{m}_l=\dfrac{\boldsymbol{u}^*_{com}+\boldsymbol{u}^*_{diff}}{V_{dc}}\end{cases} \tag{24}$$

Then, linearizing the equation yields the small-signal model:

$$\Delta\dot{\boldsymbol{x}}^{ss}(t)=\boldsymbol{A}^{ss}\Delta\boldsymbol{x}^{ss}(t)+\Delta\boldsymbol{A}^{ss}(t)\boldsymbol{X}^{ss}+\boldsymbol{B}^{ss}\Delta\boldsymbol{u}^{ss}(t) \tag{25}$$

where Δ represents the small-signal form of the variable. The details of $\boldsymbol{X}^{ss}$ is provided in the Supplementary Material. u^*_{diff} is constant under AVCM1, and u^*_{com} is $0.5U_{dc}$. Therefore, the small-signal linearization forms of $\boldsymbol{m}_u$ and $\boldsymbol{m}_l$ are 0. Then, (25) under AVCM1 can be revised to:

$$\Delta\dot{\boldsymbol{x}}^{ss}(t)=\boldsymbol{A}^{ss}\Delta\boldsymbol{x}^{ss}(t)+\boldsymbol{B}^{ss}\Delta\boldsymbol{u}^{ss}(t) \tag{26}$$

The injected perturbation frequency ω_{pert} results in a succession of small-signal harmonic components with frequencies $\omega_{pert}\pm k\omega_1$, and $k=1,2,\ldots,n$ is critical. Based on the fact that the harmonics to ±4 orders can ensure impedance model accuracy [8], the state variables can be calculated by (27) using the Fourier series expansion of the state equations in the small-signal form.

$$\Delta\boldsymbol{x}^{hss}_{pert}=(\Delta\boldsymbol{N}^{hss}_{pert}-\boldsymbol{A}^{hss})^{-1}\boldsymbol{B}^{hss}\Delta\boldsymbol{u}^{hss}_{pert} \tag{27}$$

where $\boldsymbol{A}^{hss}$ and $\boldsymbol{B}^{hss}$ are the Toeplitz matrices. The details of matrices $\Delta\boldsymbol{N}^{hss}_{pert}$ and $\Delta\boldsymbol{u}^{hss}_{pert}$ are provided in the Supplementary Material. The matrix $\boldsymbol{A}^{hss}$ is:

$$\boldsymbol{A}^{hss}=\begin{bmatrix}A_0 & A_{-1} & \cdots & A_{-4}\\ A_1 & A_0 & \cdots & A_{-3}\\ \vdots & \vdots & & \vdots\\ A_4 & A_3 & \cdots & A_0\end{bmatrix} \tag{28}$$

The small-signal impedance is obtained by dividing the +1 and −1 order harmonic currents by the perturbation voltage as:

$$\begin{cases}Z_{pos}=\dfrac{V_{s+1}(\omega_{pert})}{I_{s+1}(\omega_{pert})}\\ Z_{neg}=\dfrac{V_{s-1}(\omega_n)}{I_{s-1}(\omega_n)}\end{cases} \tag{29}$$

where the subscripts *pos* and *neg* indicate positive and negative sequences, respectively; and ω_{pert} is the positive-sequence angular frequency.

2) Impedance Modeling of WFMMC Under AVCM2

When AVCM2 is adopted, the influence of the small disturbance component introduced by the AC voltage closed loop on the upper- and lower-arm modulation indices must be considered. When the effects of the CCSC and control delay are considered, the transfer functions of the control system are expanded into harmonic transfer functions (HTFs), which are:

$$\begin{cases}\boldsymbol{H}_v=\mathrm{diag}\left[\left(K_{pvl}+\dfrac{K_{ivl}}{s-\mathrm{j}k\omega_1}\right)\right]_{9\times9}\\ \boldsymbol{H}_{cc}=\mathrm{diag}\left[\left(K_{pccl}+\dfrac{K_{iccl}}{s-\mathrm{j}k\omega_1}\right)\right]_{9\times9}\\ \boldsymbol{G}_d=\mathrm{diag}\left[\mathrm{e}^{-(s-\mathrm{j}k\omega_1)T_d}\right]_{9\times9}\end{cases} \tag{30}$$

where $k=-4,-3,\ldots,4$ represents harmonic orders; $\boldsymbol{H}_v$ and $\boldsymbol{H}_{cc}$ are the harmonic transfer functions of the voltage loop and CCSC, respectively; and $\boldsymbol{G}_d$ is the transfer function matrix of time delay. $\Delta\boldsymbol{u}^*_{diff}$ can be expressed as:

$$\begin{aligned}\Delta\boldsymbol{u}^*_{diff}=&-\boldsymbol{T}_{inv}\begin{bmatrix}\boldsymbol{G}_d & \\ & \boldsymbol{G}_d\end{bmatrix}\begin{bmatrix}\boldsymbol{H}_v & \\ & \boldsymbol{H}_v\end{bmatrix}\boldsymbol{T}_p Z_L\Delta\boldsymbol{i}_{gabc}-\\ &\boldsymbol{T}_{inv}\begin{bmatrix}\boldsymbol{G}_d & \\ & \boldsymbol{G}_d\end{bmatrix}\begin{bmatrix}\boldsymbol{H}_v & \\ & \boldsymbol{H}_v\end{bmatrix}\boldsymbol{T}_p\Delta\boldsymbol{u}_{gabc}\end{aligned} \tag{31}$$

Then, the transfer function from $\Delta\boldsymbol{i}_{gabc}$ to $\Delta\boldsymbol{u}^*_{diff}$ is:

$$\boldsymbol{TF}_{vc}=-\boldsymbol{T}_{inv}\begin{bmatrix}\boldsymbol{G}_d & \\ & \boldsymbol{G}_d\end{bmatrix}\begin{bmatrix}\boldsymbol{H}_v & \\ & \boldsymbol{H}_v\end{bmatrix}\boldsymbol{T}_p Z_L \tag{32}$$

The transfer function from $\Delta\boldsymbol{u}_{gabc}$ to $\Delta\boldsymbol{u}^*_{diff}$ is:

$$\boldsymbol{TF}_{v}=-\boldsymbol{T}_{inv}\begin{bmatrix}\boldsymbol{G}_d & \\ & \boldsymbol{G}_d\end{bmatrix}\begin{bmatrix}\boldsymbol{H}_v & \\ & \boldsymbol{H}_v\end{bmatrix}\boldsymbol{T}_p \tag{33}$$

Similarly, the transfer function from $\Delta\boldsymbol{i}_{comabc}$ to $\Delta\boldsymbol{u}^*_{cir}$ can be obtained as:

$$\boldsymbol{TF}_{ccsc}=-\boldsymbol{T}_{inv2n}\begin{bmatrix}\boldsymbol{G}_d & \\ & \boldsymbol{G}_d\end{bmatrix}\begin{bmatrix}\boldsymbol{H}_{ccsc} & \\ & \boldsymbol{H}_{ccsc}\end{bmatrix}\boldsymbol{T}_{p2n} \tag{34}$$

where $\boldsymbol{T}_p$, $\boldsymbol{T}_{p2n}$, $\boldsymbol{T}_{inv}$, and $\boldsymbol{T}_{inv2n}$ are consistent with the definitions given in [17] and, therefore, their explanations are omitted here.

The small-signal impedance model of the WFMMC under AVCM2 can be obtained by calculating (27) and (29).

3) Impedance Modeling of WFMMC Under AVCM3

The HTF of the inner-loop current controller is expressed as:

$$\boldsymbol{H}_c=\mathrm{diag}\left[\left(K_{pc}+\dfrac{K_{ic}}{s-\mathrm{j}k\omega_1}\right)\right]_{9\times9} \tag{35}$$

Based on the derivations in (31), $\Delta\boldsymbol{u}^*_{diff}$ can be updated as:

$$\begin{aligned}\Delta\boldsymbol{u}^*_{diff}=&\left\{-\boldsymbol{T}_{inv}\begin{bmatrix}\boldsymbol{G}_d & \\ & \boldsymbol{G}_d\end{bmatrix}\begin{bmatrix}\boldsymbol{H}_c & \\ & \boldsymbol{H}_c\end{bmatrix}\boldsymbol{T}_p-\right.\\ &\left.\boldsymbol{T}_{inv}\begin{bmatrix}\boldsymbol{G}_d & \\ & \boldsymbol{G}_d\end{bmatrix}\begin{bmatrix}\boldsymbol{H}_c & \\ & \boldsymbol{H}_c\end{bmatrix}\begin{bmatrix}\boldsymbol{H}_v & \\ & \boldsymbol{H}_v\end{bmatrix}\boldsymbol{T}_p Z_L\right\}\Delta\boldsymbol{i}_{gabc}-\\ &\boldsymbol{T}_{inv}\begin{bmatrix}\boldsymbol{G}_d & \\ & \boldsymbol{G}_d\end{bmatrix}\begin{bmatrix}\boldsymbol{H}_c & \\ & \boldsymbol{H}_c\end{bmatrix}\begin{bmatrix}\boldsymbol{H}_v & \\ & \boldsymbol{H}_v\end{bmatrix}\boldsymbol{T}_p\Delta\boldsymbol{u}_{gabc}\end{aligned} \tag{36}$$

$\boldsymbol{TF}_{vc}$ and $\boldsymbol{TF}_v$ are updated to:

$$\begin{cases}\boldsymbol{TF}_{vc}=-\boldsymbol{T}_{inv}\begin{bmatrix}\boldsymbol{G}_d & \\ & \boldsymbol{G}_d\end{bmatrix}\begin{bmatrix}\boldsymbol{H}_v & \\ & \boldsymbol{H}_v\end{bmatrix}\boldsymbol{T}_p-\\ \qquad\boldsymbol{T}_{inv}\begin{bmatrix}\boldsymbol{G}_d & \\ & \boldsymbol{G}_d\end{bmatrix}\begin{bmatrix}\boldsymbol{H}_c & \\ & \boldsymbol{H}_c\end{bmatrix}\begin{bmatrix}\boldsymbol{H}_v & \\ & \boldsymbol{H}_v\end{bmatrix}\boldsymbol{T}_p Z_L\\ \boldsymbol{TF}_v=-\boldsymbol{T}_{inv}\begin{bmatrix}\boldsymbol{G}_d & \\ & \boldsymbol{G}_d\end{bmatrix}\begin{bmatrix}\boldsymbol{H}_c & \\ & \boldsymbol{H}_c\end{bmatrix}\begin{bmatrix}\boldsymbol{H}_v & \\ & \boldsymbol{H}_v\end{bmatrix}\boldsymbol{T}_p\end{cases} \tag{37}$$

Similarly, the impedance model of the WFMMC under AVCM3 can be obtained.

C. Validation of Impedance Models

To validate the previous derivation, simulation models of

the PMSG-based FPWT and WFMMC under three AVCMs are constructed using MATLAB/Simulink. We use a positive sequence as an example and adopt the frequency scanning method to measure the AC-side small-signal impedances of the PMSG-based FPWT. In addition, the WFMMC is measured by injecting perturbations at the PCC [18].

As shown in Fig. 8, the measured impedances of the two systems match well with the analytical results over the entire frequency range, confirming the accuracy of the impedance models.

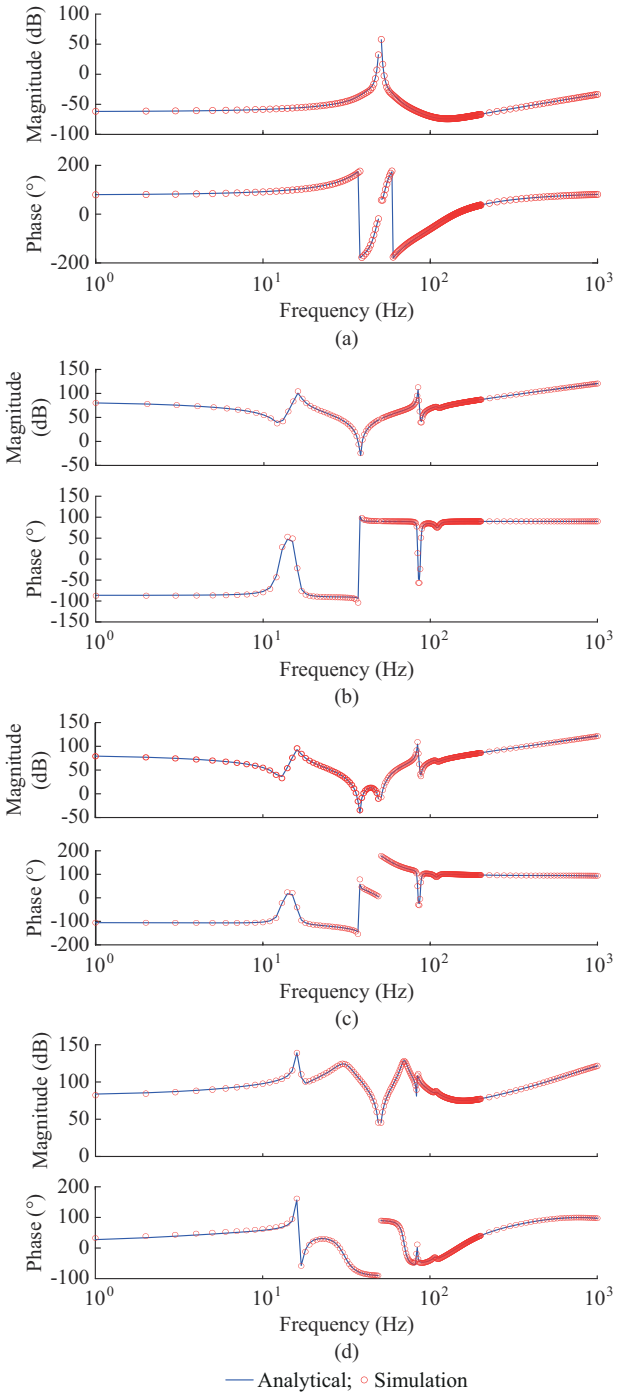

Fig. 8. Impedance model validations. (a) AC-side admittance of PMSG-based FPWT. (b) WFMMC under AVCM1. (c) WFMMC under AVCM2. (d) WFMMC under AVCM3.

V. Impacts of Different AVCMs on Stability of Interconnected System

The impacts of different AVCMs of the WFMMC on the small-signal stability of the offshore WFMMC system are analyzed and compared using the impedance-based method.

A. Comparison of Sub-/super-synchronous Stability

Figure 9 shows the impacts of different AVCMs of WFMMC on sub-/super-synchronous stability of interconnected system under different power-level conditions, where the control delay of the WFMMC is set to be 300 μs. The non-passive regions refer to the parts of the impedance phase curve that are greater than 90° but less than 180° and greater than −180° but less than −90°. Figure 9 shows that the risk of sub-/super-synchronous oscillation mainly includes two frequency bands. ① The blue area, which appears symmetrical to the fundamental frequency by 10 Hz and 80 Hz, mainly derives from WFMMC internal dynamics; this area is more prone to intersect with the wind farm impedance amplitude frequency curve, resulting in the risk of sub-/super-synchronous oscillation. ② The yellow area, which appears symmetrical to the fundamental frequency by 30 Hz and 60 Hz, mainly derives from the WFMMC current inner loop under AVCM3; this area is more prone to intersect with the wind farm impedance amplitude frequency curve, resulting in the risk of sub-/super-synchronous oscillation.

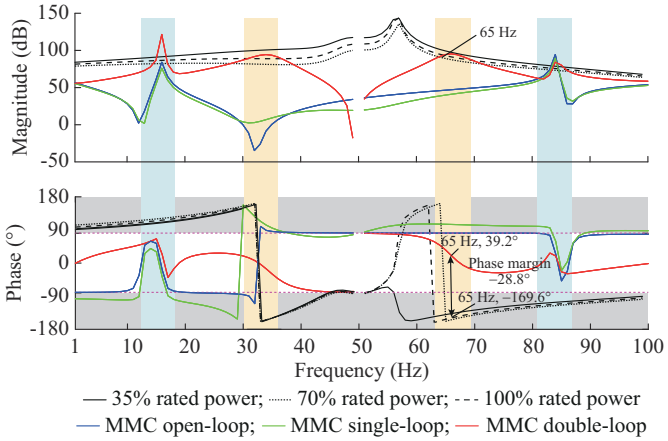

Fig. 9. Impacts of different AVCMs of WFMMC on sub-/super-synchronous stability of interconnected system.

The WFMMC impedance characteristics of AVCM1 and AVCM2 are clearly similar, whereas the WFMMC impedance magnitude curve of AVCM3 is higher than those of the other two strategies, and two resonance peaks exist around the fundamental frequency. Both the wind farm and WFMMC impedances have nonpassive regions, whereby harmonic instability is more likely to occur. Based on the frequency-domain passivity theory [19], the system is unstable when it has a phase margin of less than zero at which the two impedance magnitudes intersect. In addition, the magnitude of the wind farm impedance decreases, corresponding to an increase in wind farm output active power. Here, the WFMMC impedance magnitude of AVCM3 is more prone to intersect with that of the offshore wind farms under the

same power level conditions in the sub-/super-synchronous frequency range.

B. Comparison of Mid-/high-frequency Stability

The main reason for mid-/high-frequency oscillations in the WFMMC system is the control delay of the WFMMC [20]. Figure 10 compares the impacts of different WFMMC AVCMs on the mid-/high-frequency stability of the interconnected system, where the control delay of the WFMMC is set to be 600 μs and the wind farm output active power is 10% of the rated power. Note that the horizontal axis (frequency) of Fig. 10 adopts logarithmic coordinates.

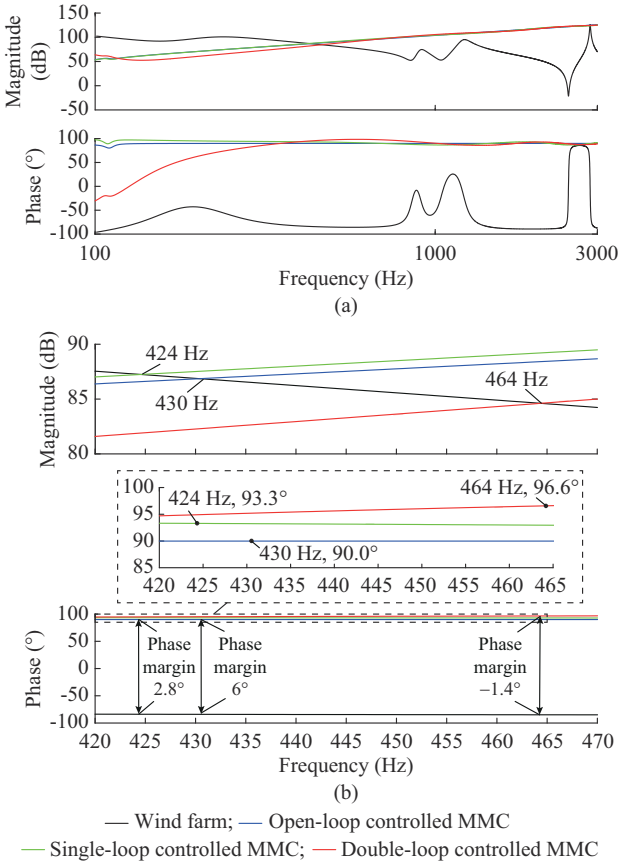

Fig. 10. Impact of different WFMMC AVCMs on mid-/high-frequency stability of interconnected system. (a) Global view. (b) Enlarged view of impedance intersection area.

Because no time delay occurs under AVCM1, its phase margin is the largest of the three AVCMs. Compared with the double-loop-controlled MMC, single- and open-loop-controlled MMCs help mitigate the risks of mid-/high-frequency oscillations.

The control methods, network, HVDC interface transformer, and controller interaction pathways are responsible for mid-/high-frequency stability. We use the WFMMC under AVCM3 as an example. Figure 11 shows the impact of control modes of WFMMC and interaction on mid-/high-frequency stability of the interconnected system, where the control delay of the WFMMC is set to be 400 μs and the wind farm output active power is 10% of the rated power. Figure 11 shows that when the current inner-loop bandwidth of the MMC is set to be 300 Hz, the magnitude-frequency curve of the wind farm intersects with that of the WFMMC at 490 Hz, where the phase margin of the interconnected system is less than zero, indicating that the system will undergo mid-/high-frequency oscillation. In addition, the system stability margin is clearly greater than zero when WFMMC adopts AVCM2, indicating that the system is stable.

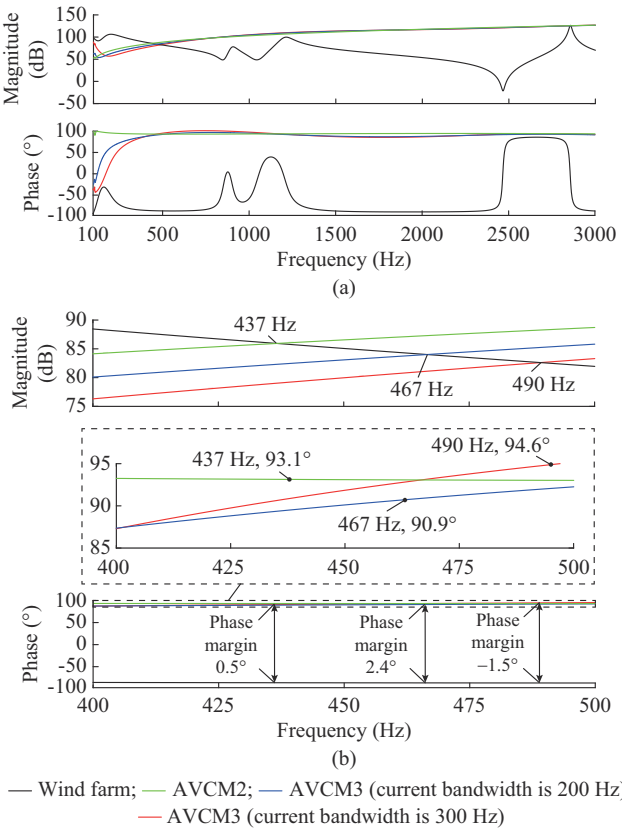

Fig. 11. Impact of control modes of WFMMC and interaction on mid-/high-frequency stability of interconnected system. (a) Global view. (b) Enlarged view of impedance intersection area.

C. Impacts of Control Interaction on Stability of Interconnected System

We next use the WFMMC under AVCM3 as an example. Figure 12 shows the impact of the current controller bandwidth of the WFMMC on the sub-/super-synchronous stability of the interconnected system. As the current bandwidth increases, the Nyquist curve changes from a stable to an unstable state that encloses point (−1, j0). In other words, the larger the current inner-loop bandwidth of the WFMMC, the greater is the risk of sub-/super-synchronous oscillation in the interconnected system.

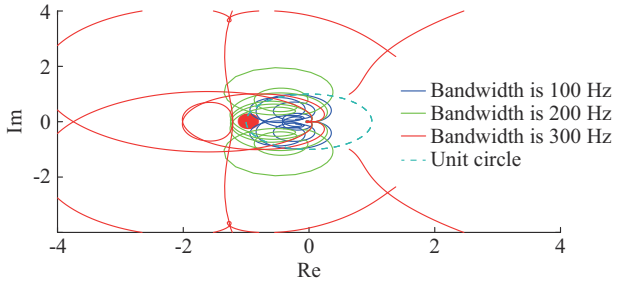

Fig. 12. Impact of current controller bandwidth of WFMMC on sub-/super-synchronous stability of interconnected system.

VI. Cases Studies

Case studies based on practical Rudong MMC-HVDC-connected offshore wind farms in China are conducted to validate the theoretical analysis.

A. Case 1: Change of Operation Points

Case 1 compares the dynamic response performances of the three AVCMs of the WFMMC when the output active power of the wind farm exhibits a step change from 0.4 p.u. to 0.6 p.u. at 1.5 s.

In Fig. 13, the simulation results of the voltage root mean square (RMS) value V_{rms} and current RMS value I_{rms} at the PCC are presented when the output active power of the wind farm changes. Figure 13 shows that the response speed of the WFMMC under AVCM1 and AVCM2 is better than that of AVCM3. In terms of control accuracy, the voltage and current of the WFMMC under AVCM1 are not as accurate as those under AVCM2 and AVCM3. When the output active power of the wind farm changes, the current overshoots at the PCC are the highest and smallest under AVCM2 and AVCM3, whereas the voltage overshoots at the PCC are the highest and smallest under AVCM3 and AVCM2. The results indicate that the WFMMC under AVCM3 has a worse voltage control effect but better current control performance under varying operating conditions.

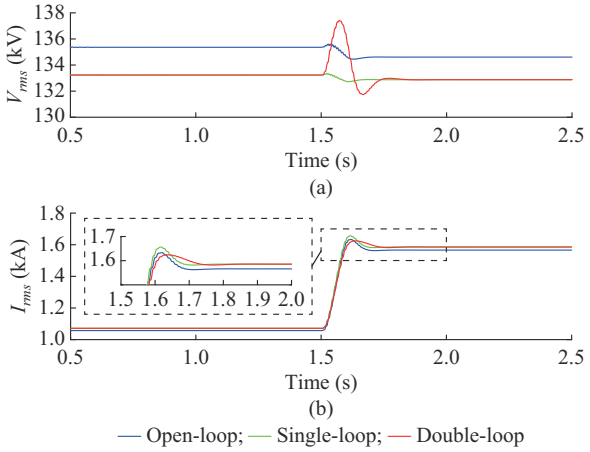

Fig. 13. Time-domain simulation results of dynamic response of tested system. (a) V_{rms}. (b) I_{rms}.

B. Case 2: Sub-/super-synchronous Stability

Case 2 is conducted to validate the theoretical analysis of the impact of three AVCMs of the WFMMC on the sub-/super-synchronous stability of the tested system, where the wind farm output active power is 70% of the rated power.

Based on the frequency-domain passivity theory, the system is unstable when it has a phase margin of less than zero at the location where two impedance magnitudes intersect in the non-passive region. Figure 9 shows that the impedance magnitudes of the wind farm and WFMMC under AVCM3 intersect at 65 Hz when the impedance of the wind farm falls in the non-passive region, indicating that the system will be unstable at 65 Hz. Nevertheless, the impedance magnitudes of the WFMMC under the other two AVCMs do not intersect with that of the wind farm under the same operating conditions, indicating that the system is stable.

The simulation results for Case 2 are conducted with a power output of 70%, as shown in Fig. 14, which shows that the tested system is stable under AVCM1 and AVCM2 of the WFMMC, whereas the system oscillates under AVCM3. Note that THD in Fig. 14 stands for total harmonic distortion. The dominant oscillation frequency of the PCC current is approximately 65 Hz, as observed from the frequency analysis, which is consistent with the theoretical analysis presented in Fig. 9. In addition, because of the mirror frequency-coupling effect, a frequency component at 35 Hz is produced [23].

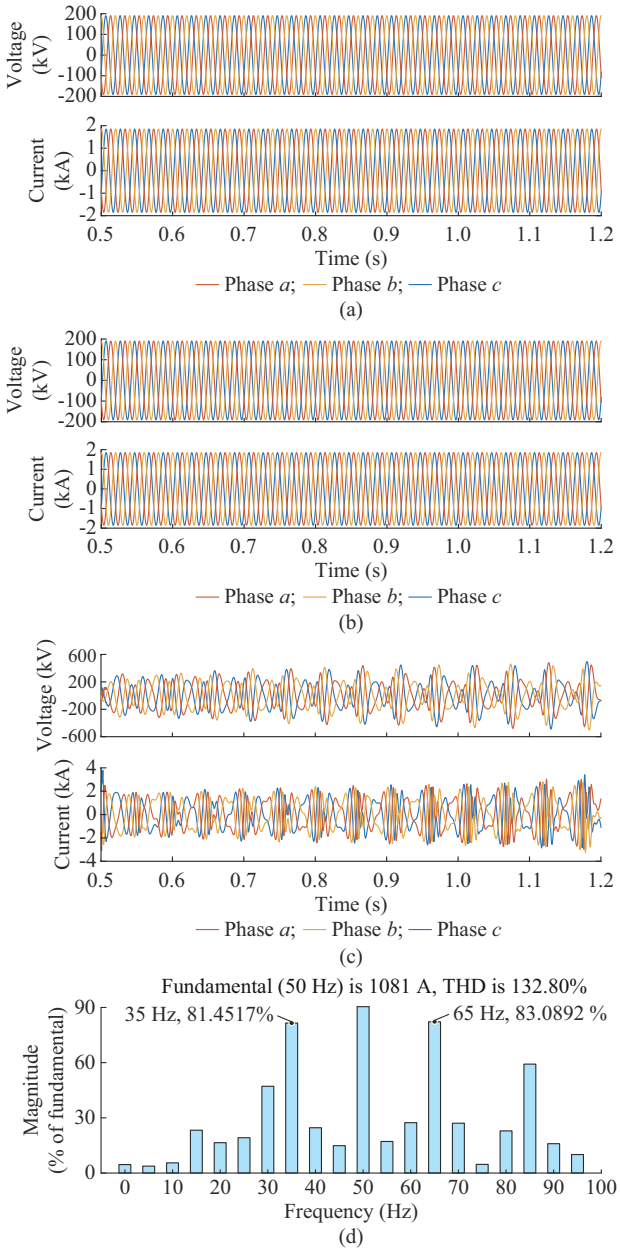

Fig. 14. Simulation results for Case 2. (a) Three-phase voltages and currents at PCC under AVCM1. (b) Three-phase voltages and currents at PCC under AVCM2. (c) Three-phase voltages and currents at PCC under AVCM3. (d) Frequency analysis of PCC current.

C. Case 3: Mid-/high-frequency Stability

1) Case 3.1: Impact of WFMMC Control Delay

Case 3.1 is conducted to validate the theoretical analysis of the impact of the WFMMC control delay under three AVCMs on the mid-/high-frequency stability of the interconnected system. The operating conditions are the same as those shown in Fig. 10. Figure 10 shows that under AVCM3, the phase margin of the tested system at the intersection (464 Hz) of the impedance magnitude curves is −1.4°, indicating that the system will be unstable. By contrast, the phase margins of the system under AVCM1 and AVCM2 are greater than zero, indicating that the system will be stable.

The simulation results for Case 3.1 are shown in Fig. 15. As the WFMMC control delay increases to 600 μs at 1 s, the system under AVCM2 remains stable, whereas the system under AVCM3 oscillates at 464 Hz, which is in agreement with the theoretical analysis presented in Fig. 10.

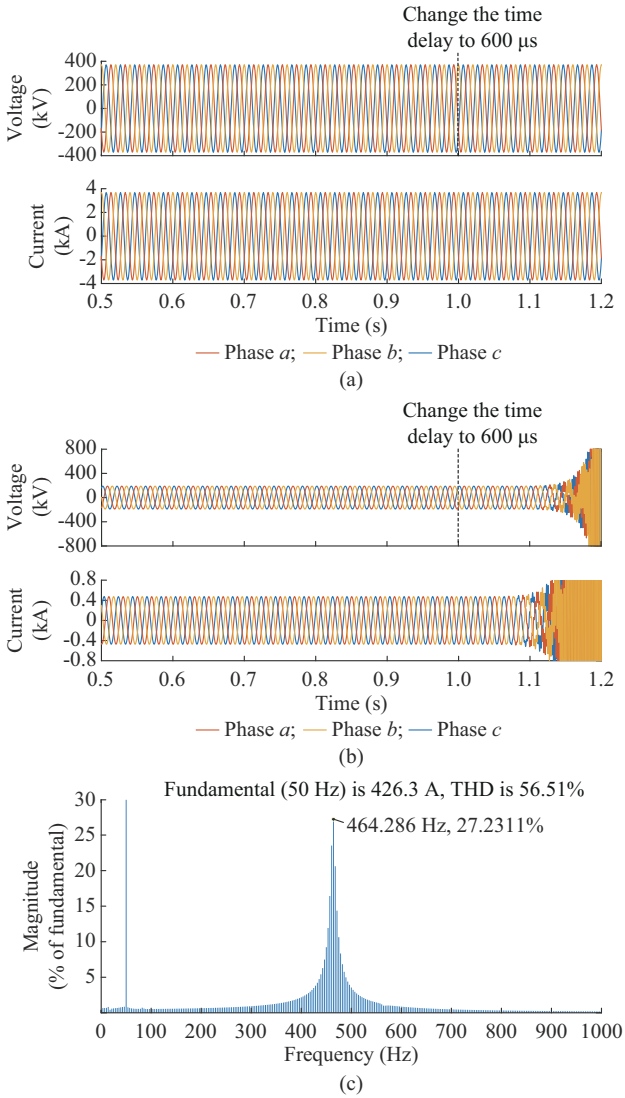

Fig. 15. Simulation results for Case 3.1. (a) Three-phase voltages and currents at PCC under AVCM2. (b) Three-phase voltages and currents at PCC under AVCM3. (c) Frequency analysis of PCC current.

2) Case 3.2: Impact of WFMMC Control Modes

Case 3.2 is conducted to compare the impact of different WFMMC control modes on the mid-/high-frequency stability of the interconnected system. The theoretical analysis is presented in Fig. 11. The WFMMC initially operates under AVCM3 with a 300 Hz current inner-loop bandwidth. The time-domain simulation results in Fig. 16 show that when the WFMMC is switched to the AVCM2 at 0.8 s, the mid-/high-oscillation phenomenon of the interconnected system gradually disappears and the system returns to normal operation, which is consistent with the theoretical analysis presented in Fig. 11.

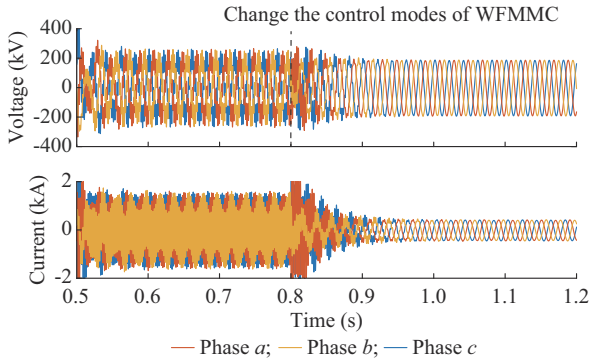

Fig. 16. Simulation results in different control modes for Case 3.2, showing three-phase voltages and currents at PCC.

D. Case 4: Control Interaction Between Wind Farm and WFMMC

1) Case 4.1: Sub-/super-synchronous Stability

Case 4.1 is conducted to validate the analysis of control interaction on the sub-/super-synchronous stability of the interconnected system. Figure 12 shows that when the WFMMC current inner-loop bandwidth is set to be 200 Hz, the Nyquist curve encloses (–1, j0), indicating an unstable state. When the current inner-loop bandwidth is reduced to 100 Hz, the Nyquist curve changes from an unstable to a stable state.

The simulation results in different control modes for Case 3.2 are shown in Fig. 17. When the current inner-loop bandwidth is reduced from 200 Hz to 100 Hz, the system becomes stable, verifying the previous theoretical analysis.

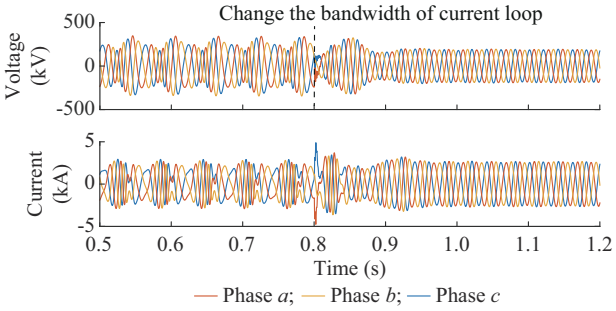

Fig. 17. Simulation results in different control modes for Case 3.2.

2) Case 4.2: Mid-/high-stability

Case 4.2 is conducted to validate the theoretical analysis of control interaction on the mid-/high-stability of the interconnected system. The simulation results under different current inner-loop bandwidths for Case 4.2 are shown in Fig.

18. Figure 18 shows that when the current inner-loop bandwidth is increased to 1 s, the system becomes unstable. In addition, the dominant oscillation frequency of the PCC current is approximately 490 Hz, as observed from the frequency analysis, which is consistent with the theoretical analysis presented in Fig. 11.

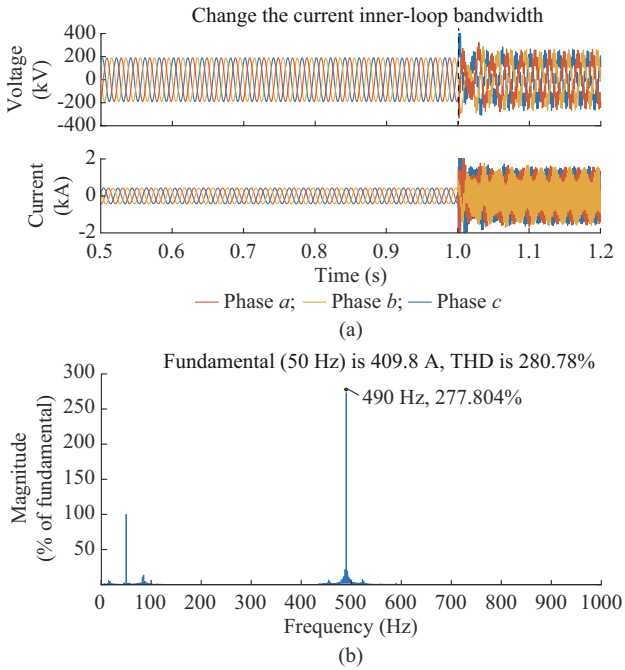

Fig. 18. Simulation results under different current inner-loop bandwidths for Case 4.2. (a) Three-phase voltages and currents at PCC under AVCM3. (b) Frequency analysis of the PCC current.

VI. Conclusion

This paper presents a comparative study of different AVCMs of a WFMMC in terms of control performance and small-signal stability of MMC-HVDC-connected offshore wind farms. The main conclusions of this paper are summarized as follows.

1) Single- and double-loop AC voltage controls are shown to have better control accuracy and more auxiliary functions as compared with the open-loop control. The double-loop-controlled WFMMC is affected to a greater extent by the wind farm output active power, whereas the single-loop controlled MMC is less affected.

2) In both sub-/super-synchronous and mid-/high-frequency ranges, the double-loop AC-voltage-controlled WFMMC is shown to have a higher risk of oscillation as compared with the open- and single-loop AC-voltage-controlled WFMMCs.

3) In terms of small-signal stability, the single-loop controlled MMC is shown to be the best choice for reducing the oscillation risk of MMC-HVDC systems.

References

[1] V. Yaramasu, B. Wu, P. C. Sen *et al*., "High power wind energy conversion systems: state-of-the-art and emerging technologies," *Proceedings of the IEEE*, vol. 103, no. 5, pp. 740-788, May 2015.

[2] J. Lyu, X. Cai, and M. Molinas, "Sub-synchronous oscillation mechanism and its suppression in MMC-based HVDC connected wind farms," *IET Generation, Transmission & Distribution*, vol. 12, no. 4, pp. 1021-1029, Feb. 2018.

[3] L. P. Kunjumuhammed, B. C. Pal, R. Gupta *et al*., "Stability analysis of a PMSG-based large offshore wind farm connected to a VSC-HVDC," *IEEE Transactions on Energy Conversion*, vol. 32, no. 3, pp. 1166-1176, Sept. 2017.

[4] J. Lyu, X. Cai, and M. Molinas, "Frequency domain stability analysis of MMC-based HVDC for wind farm integration," *IEEE Journal of Emerging & Selected Topics in Power Electronics*, vol. 4, no. 1, pp. 141-151, Mar. 2016.

[5] F. Feng, J. Yu, W. Dai *et al*., "Operational reliability model of hybrid MMC considering multiple time scales and multi-state submodule," *Journal of Modern Power Systems and Clean Energy*, vol. 9, no. 3, pp. 648-656, May 2021.

[6] H. Lin, J. Lyu, D. Zhai *et al*., "Comparative analysis of impact of wind farm side MMC with different AC voltage control strategies on the stability of MMC-HVDC connected wind farm," in *Proceedings of The 10th Renewable Power Generation Conference (RPG 2021)*, virtual conference, Oct. 2021, pp. 1039-1045.

[7] J. Lyu, X. Cai, and M. Molinas, "Optimal design of controller parameters for improving the stability of MMC-HVDC for wind farm integration," *IEEE Journal of Emerging & Selected Topics in Power Electronics*, vol. 6, no. 1, pp. 40-53, Mar. 2018.

[8] J. Lyu, X. Zhang, X. Cai *et al*., "Harmonic state-space based small-signal impedance modeling of a modular multilevel converter with consideration of internal harmonic dynamics," *IEEE Transactions on Power Electronics*, vol. 34, no. 3, pp. 2134-2148, Mar. 2019.

[9] H. Wu, X. Wang, and L. H. Kocewiak, "Impedance-based stability analysis of voltage-controlled MMCs feeding linear AC systems," *IEEE Journal of Emerging & Selected Topics in Power Electronics*, vol. 8, no. 4, pp. 4060-4074, Dec. 2020.

[10] X. Xiong, Y. Yang, C. Wu *et al*., "Improving the stability of standalone MMCs by shaping the AC side impedance using insertion index compensation," *IEEE Journal of Emerging & Selected Topics in Power Electronics*, vol. 12, no. 1, pp. 81-89, Mar. 2022.

[11] T. Huang, F. Yang, D. Zhang *et al*., "High-frequency stability analysis and impedance optimization for an MMC-HVDC integrated system considering delay effects," *IEEE Journal of Emerging & Selected Topics in Power Electronics*, vol. 12, no. 1, pp. 59-72, Mar. 2022.

[12] T. Li, A. M. Gole, and C. Zhao, "Harmonic instability in MMC-HVDC converters resulting from internal dynamics," *IEEE Transactions on Power Delivery*, vol. 31, no. 4, pp. 1738-1747, Aug. 2016.

[13] M. Beza and M. Bongiorno, "Identification of resonance interactions in offshore-wind farms connected to the main grid by MMC-based HVDC system," *International Journal of Electrical Power & Energy Systems*, vol. 111, no. 1, pp. 101-113, Feb. 2019.

[14] H. Zong, C. Zhang, J. Lyu *et al*., "Generalized MIMO sequence impedance modeling and stability analysis of MMC-HVDC with wind farm considering frequency couplings," *IEEE Access*, vol. 8, pp. 55602-55618, Mar. 2020.

[15] K. Ji, G. Tang, J. Yang *et al*., "Harmonic stability analysis of MMC-based DC system using DC impedance model," *IEEE Journal of Emerging & Selected Topics in Power Electronics*, vol. 8, no. 2, pp. 1152-1163, Jun. 2020.

[16] P. Li, Y. Wang, X. Li *et al*., "DC impedance modeling and design-oriented harmonic stability analysis of MMC-PCCF-based HVDC system," *IEEE Transactions on Power Electronics*, vol. 37, no. 4, pp. 4301-4319, Apr. 2022.

[17] T. Xue, J. Lyu, H. Wang *et al*., "A complete impedance model of a PMSG-based wind energy conversion system and its effect on the stability analysis of MMC-HVDC connected offshore wind farms," *IEEE Transactions on Energy Conversion*, vol. 36, no. 4, pp. 3449-3461, Dec. 2021.

[18] M. Jaksic, Z. Shen, I. Cvetkovic *et al*., "Wide-bandwidth identification of small-signal DQ impedances of AC power systems via single-phase series voltage injection," in *Proceedings of European Conference on Power Electronics & Applications (IEEE)*, Geneva, Switzerland, Apr. 2015, pp. 1-10.

[19] Y. Rao, J. Lyu, D. Zhai *et al*., "An adaptive wideband oscillation suppression method for wind farm integration through MMC-HVDC system," in *Proceedings of the 10th Renewable Power Generation Conference (RPG 2021)*, virtual conference, Oct. 2021, pp. 44-51.

[20] L. Harnefors, X. Wang, A. G. Yepes *et al*., "Passivity-based stability assessment of grid-connected VSCs – an overview," *IEEE Journal of Emerging & Selected Topics in Power Electronics*, vol. 4, no. 1, pp. 116-126, Mar. 2016.

[21] A. Rygg, M. Molinas, C. Zhang *et al*., "A modified sequence-domain

impedance definition and its equivalence to the *dq*-domain impedance definition for the stability analysis of AC power electronic systems," *IEEE Journal of Emerging & Selected Topics in Power Electronics*, vol. 4, no. 4, pp. 1383-1396, Dec. 2016.

Hongfei Lin received the B.Eng. degree in electrical engineering and automation from the Northeast Electric Power University, Jilin, China, in 2020. He is currently pursuing the M.Eng. degree in Shanghai Jiao Tong University, Shanghai, China. His research interests include stability analysis and control of modular multilevel converter based high voltage direct current (MMC-HVDC) connected wind farms.

Tao Xue received the B.Eng. degree in electrical engineering and automation from North China Electric Power University, Beijing, China, in 2018, and the M.Eng. degree in electrical engineering from Shanghai Jiao Tong University, Shanghai, China, in 2021. He is currently pursuing the Ph.D. degree at the Department of Electrical Engineering, The Hong Kong Polytechnic University, Hong Kong, China. His research interests include the safe operation of AC/DC transmission systems with massive inverter-based renewables integration.

Jing Lyu received the M.Eng. and Ph.D. degrees from Shanghai Jiao Tong University, Shanghai, China, in 2011 and 2016, respectively. He was a Postdoctoral Research Fellow with the Department of Engineering Cybernetics, Norwegian University of Science and Technology, Trondheim, Norway, from 2016 to 2017. Since 2018, he has been with the Department of Electrical Engineering, Shanghai Jiao Tong University, where he is currently a tenure-track Associate Professor. His research interests include stability analysis and control of high voltage direct current (HVDC) connected renewable energy, application of artificial intelligence in wind power systems.

Xu Cai received the M.Eng. and Ph.D. degrees from China University of Mining and Technology, Xuzhou, China, in 1988 and 2000, respectively, both in electrical engineering. He was with the Department of Electrical Engineering, China University of Mining and Technology, as an Associate Professor from 1989 to 2001. He was the Vice Director of the State Energy Smart Grid R&D Center, Shanghai, China, from 2010 to 2013. He has been with Shanghai Jiao Tong University, Shanghai, China as a Professor since 2002, where he has also been the Director of the Wind Power Research Center since 2008. His research interests include large power electronics, wind power generation and grid integration, high-voltage direct current, large power battery storage systems.